



# Interfacial modification of $\text{La}_{0.80}\text{Sr}_{0.20}\text{MnO}_{3-\delta}$ – $\text{Er}_{0.4}\text{Bi}_{0.6}\text{O}_3$ cathodes for high performance lower temperature solid oxide fuel cells

Kang Taek Lee<sup>a,c</sup>, Doh Won Jung<sup>b</sup>, Hee Sung Yoon<sup>a</sup>, Ashley A. Lidie<sup>a</sup>, Matthew A. Camaratta<sup>c</sup>, Eric D. Wachsman<sup>a,\*</sup>

<sup>a</sup> University of Maryland Energy Research Center, University of Maryland, College Park, MD 20742, USA

<sup>b</sup> Samsung Advanced Institute of Technology, Yongin-si, Republic of Korea

<sup>c</sup> Department of Materials Science and Engineering, University of Florida, Gainesville, FL 32611, USA

## H I G H L I G H T S

- Using a highly conductive ESB, the LSM cathode/electrolyte interface is functionally modified.
- Cathodic polarization with an ESB layer is reduced by 60% due to enhanced oxygen incorporation.
- The maximum power density of a SOFC using this modification is over  $1 \text{ W cm}^{-2}$  at  $650^\circ\text{C}$ .
- The SOFC shows a stable performance for  $\sim 200 \text{ h}$ .

## A R T I C L E I N F O

### Article history:

Received 28 June 2012

Received in revised form

31 July 2012

Accepted 1 August 2012

Available online 9 August 2012

### Keywords:

Lower temperature solid oxide fuel cells

Stabilized bismuth oxides

Lanthanum strontium manganese oxides

High performance cathodes

## A B S T R A C T

The performance of conventional  $\text{La}_{0.80}\text{Sr}_{0.20}\text{MnO}_{3-\delta}$  (LSM) cathodes was dramatically improved using a highly conductive  $\text{Er}_{0.4}\text{Bi}_{0.6}\text{O}_3$  (ESB) phase. ESB was utilized not only as the ion-conducting phase in the LSM–ESB cathode, but also as an electrolyte coupled to the LSM–ESB cathode. The electrode area specific resistance (ASR) measured from a symmetric cell consisting of LSM–ESB electrodes on an ESB electrolyte was only  $0.43 \Omega \text{ cm}^2$  at  $600^\circ\text{C}$ , which is  $\sim 60\%$  lower than that of identical LSM–ESB cathodes on  $\text{Gd}_{0.1}\text{Ce}_{0.9}\text{O}_{1.95}$  (GDC) electrolytes ( $1.11 \Omega \text{ cm}^2$ ). Deconvolution of the impedance spectra reveals that this significantly smaller cathode ASR with an ESB electrolyte is due to a higher rate of oxygen incorporation at the cathode/ESB electrolyte interface. The maximum power density (MPD) of an anode-supported solid oxide fuel cell (SOFC) with an LSM–ESB cathode on an ESB|GDC bilayered electrolyte reached  $\sim 1013 \text{ mW cm}^{-2}$  at  $650^\circ\text{C}$ . The measured MPDs at low temperatures, from  $450$  to  $650^\circ\text{C}$ , are to date the highest reported values for SOFCs using LSM-based composite cathodes.

© 2012 Elsevier B.V. All rights reserved.

## 1. Introduction

$\text{La}_{1-x}\text{Sr}_x\text{MnO}_{3-\delta}$  (LSM)-based cathodes are some of the most widely used cathodes for high temperature ( $>800^\circ\text{C}$ ) solid oxide fuel cells (SOFCs) due to their high thermal and chemical stability and electrical conductivity. LSM-based cathodes exhibit good compatibility with conventional electrolyte materials, such as stabilized zirconia and doped ceria [1–4]. Despite these advantages, LSM-based cathodes are not a popular choice for reduced temperature ( $<800^\circ\text{C}$ ) SOFCs. LSM has negligible ionic conductivity and a high activation

energy for the oxygen reduction reaction (ORR), leading to significantly diminished electrochemical performance at low temperatures [5–8]. Moreover, recent isothermal isotope exchange studies have demonstrated that oxygen incorporation into the lattice is the rate limiting step for LSM, even though it is quite facile for the dissociative adsorption of oxygen molecules on the surface [9,10].

To overcome this limitation, conventional ionic conducting phases such as yttria-stabilized zirconia (YSZ) and gadolinia-doped ceria (GDC) have been mixed with LSM leading to improved electrochemical performance [2,10–16]. Thus it is expected that dual phase cathodes with a higher ionic conductivity phase will yield further improvements in performance.

Erbia-stabilized bismuth oxide (ESB) has been reported to have one of the highest known ionic conductivities, 1–2 orders of magnitude higher than conventional YSZ at lower temperatures

\* Corresponding author. 1206 Engineering Lab Bldg, University of Maryland, College Park, MD 20742, USA. Tel.: +1 301 405 8193; fax: +1 301 314 8514.

E-mail address: [ewach@umd.edu](mailto:ewach@umd.edu) (E.D. Wachsman).

(<650 °C, LT) [17,18]. In addition, bismuth-oxides enhance surface oxygen exchange kinetics [19,20] including charge transfer [21] and dissociative adsorption of oxygen [22], which are the rate-limiting steps in the ORR at the cathode. For example, isotope exchange experiments by Steele et al. resulted in significantly higher (a factor of  $10^3$  at 700 °C) surface exchange coefficient ( $K_s$ ) of bismuth oxides compared to zirconia [22].

Similarly, electrochemical impedance results of a bismuth-ruthenate  $\text{Bi}_2\text{Ru}_2\text{O}_7$  (BRO7)–ESB composite cathode on an ESB electrolyte exhibited low ASR values of 0.73 and  $0.03 \Omega \text{ cm}^2$  at 500 and 700 °C, respectively [23,24]. However, bismuth oxides are unsuitable as a SOFC electrolyte due to their thermodynamic instability under the low oxygen pressure typical of anodic conditions [25]. In order to overcome this, an ESB|GDC bilayered electrolyte was developed [26]. Using this bilayered electrolyte with a BRO7–ESB cathode, we recently demonstrated exceptionally high power density ( $\sim 2 \text{ W cm}^{-2}$  at 650 °C) [27,28]. These results indicate that cathode performance is promoted not only by the addition of ESB as the ion conducting phase in composite cathodes but also by using an ESB electrolyte at the cathode interface due to improved oxygen incorporation into the electrolyte lattice resulting in a reduction of the cathode polarization losses.

Several studies have focused on the utilization of stabilized bismuth oxides as the ionic conducting phase in order to improve the performance of LSM-based cathodes at reduced temperature [29–38]. Moreover, various fabrication techniques were used in order to obtain increased triple phase boundary (TPB) lengths through microstructural evolution [31,32,37]. Although these efforts progressively reduced the cathode ASR, the reported power densities of SOFCs utilizing LSM–bismuth oxide cathodes are still relatively low at lower temperatures ( $\sim 600 \text{ mW cm}^{-2}$  at 650 °C) [32]. To date, the majority of studies of LSM–bismuth oxide composite cathodes have been conducted on zirconia- or ceria-based electrolytes. Even though ultra thin YSZ electrolytes decrease total ohmic polarization losses at low temperature [39], a significant decrease in ionic conduction and oxygen reduction reactivity at the cathode/electrolyte interface is inevitable due to the abrupt change in ionically conductive phase from bismuth oxide in the cathode to the zirconia electrolyte.

In this study, we introduced an ESB cathode/electrolyte interfacial layer coupled with an LSM–ESB composite cathode. To gauge the effect of the ESB electrolyte on the cathode performance, the interfacial resistance of the cathode on ESB and on GDC electrolytes was measured with symmetric cells by electrochemical impedance spectroscopy (EIS). To investigate the ORR mechanism with this cathode, we deconvoluted the impedance spectra. Finally, performance of the LSM–ESB cathode on an ESB electrolyte layer was evaluated using an anode-supported SOFC with an ESB|GDC bilayer via current–voltage ( $I$ – $V$ ) measurements.

## 2. Experimental

### 2.1. Sample fabrication

ESB powders were synthesized via a conventional solid state method. A stoichiometric mixture of  $\text{Bi}_2\text{O}_3$  (99.9995% pure) and  $\text{Er}_2\text{O}_3$  (99.99% pure) from Alfa Aesar was mixed and ball-milled with zirconia ball media for 24 h. After milling, the mixed powders were calcined at 800 °C for 16 h. Agglomerated powders were ground using mortar and pestle and sieved through 325 mesh. This ESB powder and  $\text{La}_{0.80}\text{Sr}_{0.20}\text{MnO}_{3-\delta}$  (LSM) powder from Fuel Cell Materials were mixed with the same weight ratio (50:50 wt%). The powder mixture was added to a binder system consisting of alpha terpineol, di-n-butyl phthalate and ethanol as binder, plasticizer and solvent, respectively.

To make symmetric cells, both ESB and GDC (Rhodia) electrolyte pellets were prepared by uniaxial pressing and sintered at 890 °C for 16 h and 1500 °C for 10 h, respectively. All pellets exhibited a relative density greater than 95% of the theoretical density. The LSM–ESB cathode ink was brush coated on both sides of the electrolyte substrates and sintered at 800 °C for 2 h in air.

The fabricated SOFC samples (button cells) utilized an anode-supported cell structure with an ESB|GDC bilayer electrolyte. Micron-sized NiO (Alfa Aesar)–GDC (Rhodia) (65:35 wt%) particles for the anode-support was tape-cast and an anode functional layer (AFL) consisting of submicron-sized NiO (JT Baker)–GDC (Rhodia) (60:40 wt%) particles was applied via colloidal deposition and presintered at 900 °C. A thin and uniform GDC electrolyte was deposited using spin coating at 1500 rpm for 20 s. The spin coating process was repeated until the desired thickness was obtained. The multilayer NiO–GDC|AFL|GDC structure was co-sintered at 1450 °C for 4 h. Nano-sized ESB powder was synthesized using a wet chemical coprecipitation method to establish a thin and dense ESB layer on the GDC electrolyte surface. A colloidal solution containing nano-sized ESB particles was spin-coated onto the GDC layer and sintered at 800 °C for 4 h. Detailed fabrication of the ESB|GDC bilayered electrolytes is described elsewhere [40]. After sintering the ESB layer, the LSM–ESB cathode was brush coated onto the ESB electrolyte surface and sintered at 800 °C for 2 h.

### 2.2. Characterization

The SOFC microstructure, with the LSM–ESB cathode, was characterized using scanning electron microscopy (SEM, JEOL 6400/6335F). Phase stability was investigated using X-ray diffraction analysis (XRD, Philips APD 3720). The interfacial polarization resistance of the LSM–ESB electrodes on symmetric cells was measured by two-point probe EIS using a Solartron 1260 with an AC voltage amplitude of 50 mV over the frequency range of 0.1 MHz to 0.1 Hz in air. To analyze electrochemical performance of the button cell,  $I$ – $V$  measurements were conducted with a Solartron 1407E under 90 sccm of dry air and 3% wet hydrogen to the cathode and anode side, respectively.

## 3. Result and discussion

### 3.1. Phase and microstructural analysis

Compatibility between LSM and ESB was investigated using XRD. LSM and ESB powders were mixed in a 1:1 weight ratio and annealed at 900 °C for 50 h. Fig. 1a shows the XRD patterns of the LSM–ESB powder mixture before and after annealing indicating no reactivity between the two phases up to this temperature. In contrast, ESB is highly reactive and thus incompatible with  $\text{La}_{0.6}\text{Sr}_{0.4}\text{Co}_{0.2}\text{Fe}_{0.8}\text{O}_3$  (LSCF), which is a commonly used cathode material for LT-SOFCs, even at lower temperature (850 °C) for much shorter time (1 h) as shown in Fig. 1b. Kharton et al. reported this reactivity is due to the formation of a solid solution by inter-diffusion at the cobaltite/ $\text{Bi}_2\text{O}_3$ -based oxide interface [41].

Fig. 2 shows the microstructure of the LSM–ESB composite cathode on ESB and GDC electrolytes after sintering at 800 °C for 2 h. As shown in these micrographs, the porous LSM–ESB cathodes were homogeneously mixed and well-deposited on both electrolytes.

### 3.2. Impedance spectroscopy of symmetric cells

Fig. 3 shows the impedance spectra measured under open circuit conditions from 500 to 700 °C with 50 °C intervals for LSM–ESB|ESB|LSM–ESB and LSM–ESB|GDC|LSM–ESB symmetric cells. For direct

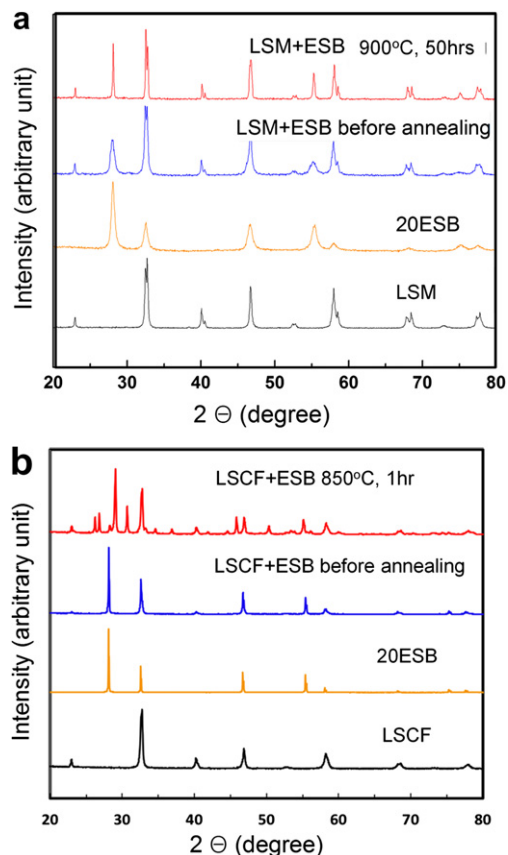


**Fig. 1.** XRD patterns showing compatibility (a) between LSM and ESB after annealing at 900 °C for 50 h and (b) between LSCF and ESB after annealing at 850 °C for 1 h.

comparison of the electrode ASRs on the different electrolytes, all of the impedance spectra were ohmic resistance-corrected. That is, the high frequency intercept at the real axis of each spectrum, which corresponds to bulk electrolyte, electrode-sheet, and lead-contact resistance, was subtracted from each data point.

The electrode ASRs of the LSM–ESB cathode on GDC at 500, 550, 600, 650, and 700 °C were 10.56, 3.31, 1.11, 0.44, and 0.19  $\Omega \text{ cm}^2$ , respectively. This result is comparable with the ASRs of the LSM–yttria stabilized bismuth oxide (YSB) cathode on samarium-doped ceria (SDC) electrolytes reported by Jiang et al. – 1.08 and 0.15  $\Omega \text{ cm}^2$  at 600 and 700 °C, respectively [31].

However, the electrode ASRs of the LSM–ESB on ESB were substantially lower – 4.18, 1.29, 0.43, 0.19, and 0.08  $\Omega \text{ cm}^2$  at 500, 550, 600, 650, and 700 °C, respectively compared to those of LSM–ESB on GDC electrolyte. The percent electrode ASR reduction of LSM–ESB on ESB relative to that on GDC is shown in Fig. 4. A constant ~60% reduction in ASR at all testing temperatures is observed. Previously we reported a similar effect with a BRO7–ESB cathode on an ESB electrolyte showing a 26% reduction of the ASR relative to that on a GDC electrolyte [28].

### 3.3. Cathodic polarization mechanism

The activation energy of LSM–ESB cathodes on GDC and on ESB was calculated from EIS data (Fig. 4) using an Arrhenius relationship. The calculated activation energies for both cells were identical, ~1.23 eV. This value is in good agreement with other reported values for LSM–bismuth oxide cathodes (1.23–1.5 eV), which of course depend on microstructure and composition of the composite cathodes [29,31,33,37]. For comparison, the activation

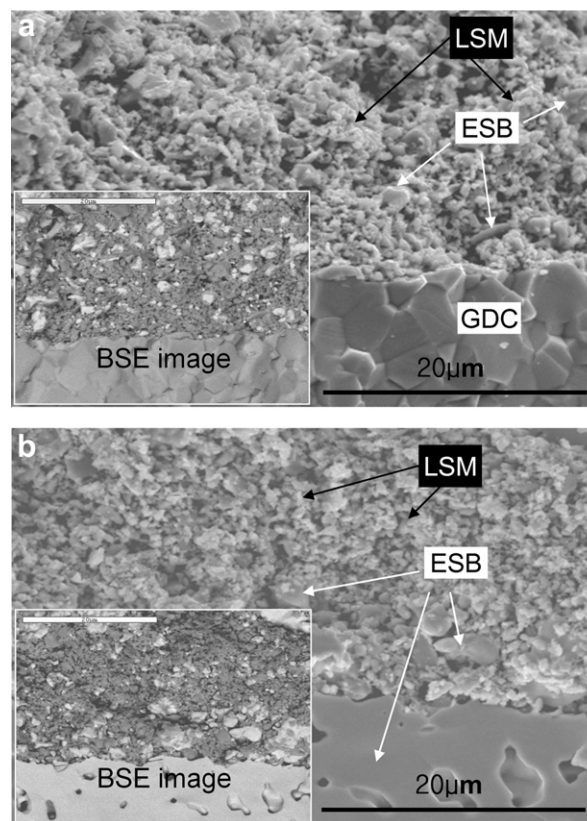


**Fig. 2.** SEM micrographs of LSM–ESB cathode on (a) GDC electrolyte and (b) ESB electrolyte. Insets show the back-scattered images (Light and dark colors in insets represent ESB and LSM respectively.).

energy for pure LSM on a SDC electrolyte is at the high end, ~1.5 eV [31]. These results indicate that even though there is a significant reduction in the magnitude of the ASR from EIS for LSM–ESB cathodes on ESB vs GDC electrolytes, the apparent overall rate limiting step is similar.

The EIS data were further analyzed by fitting the Nyquist plots with Z-plot software using the equivalent circuit shown in Fig. 5 in order to identify the ORR steps from the experimental results. In this circuit,  $L$  is the inductance from the apparatus and  $R_0$  represents the resistance of the bulk electrolyte, electrode-sheet and lead-contact resistance. An equivalent circuit of  $(R_n-CPE_n)$  was used to identify each arc of the Nyquist plot representing each electrochemical process at a specific frequency range.  $R_H$  and  $R_L$  correspond to the high and low frequency resistance, respectively while  $CPE_H$  and  $CPE_L$  represent the constant phase elements at high and low frequency, respectively. An additional high frequency arc ( $R_{H'}-CPE_{H'}$ ) was used to identify the grain boundary resistance of the GDC electrolyte at low temperature (<550 °C). The resultant fittings are overlapped with the experimental results in Fig. 3.

Fig. 6 shows the comparison between  $R_H$  and  $R_L$  for LSM–ESB cathodes on GDC and ESB. The use of ESB electrolyte versus a GDC electrolyte primarily impacts the  $R_H$  value. In the ESB electrolyte sample, the  $R_H$ s are much lower than with the GDC electrolyte cell (Fig. 6a), while the  $R_L$ s are almost identical for both electrolyte cases albeit with a difference in activation energy (Fig. 6b). Moreover, the activation energy of  $R_H$  in the LSM–ESB cathode on ESB electrolyte changed from 0.25 eV above 600 °C to 1.44 eV below 600 °C. This is typical behavior for the ESB conductivity activation energy, due to an order/disorder transition at ~600 °C resulting in an activation energy of ~0.65 eV above and ~1.22 eV below 600 °C [42]. This indicates ionic conductivity of the

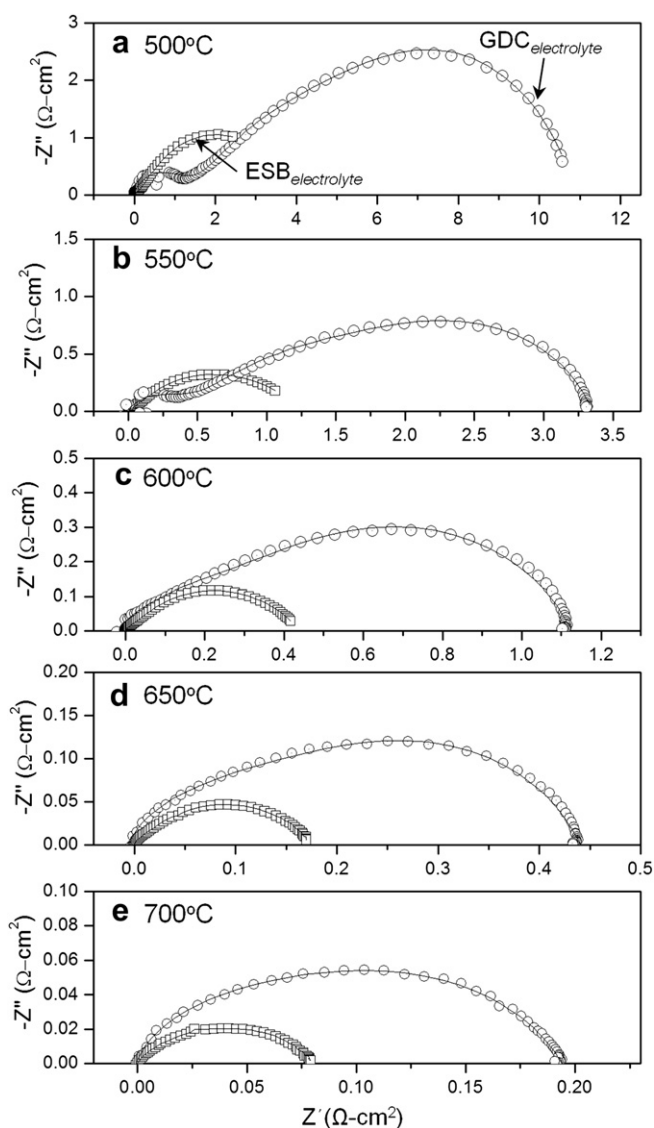


**Fig. 3.** Impedance spectra of the LSM–ESB cathode on ESB (open squares) and GDC (open circles) pellets at the temperature ranges from 500 to 700 °C. The lines represent the fitted equivalent circuit results using Z-plot (Fig. 5).

electrolyte at the cathode/electrolyte interface strongly influences  $R_H$  and has minimal effect on  $R_L$  for the LSM–ESB on ESB cell.

The low frequency arc is usually attributed to surface diffusion and dissociative adsorption of the oxygen at the cathode surface and the high frequency arc is usually attributed to incorporation of the oxygen ion into the lattice [37,43]. Thus it is not surprising that the impedance component associated with incorporation into the lattice would be influenced by the activation energy of the ion conducting phase. However, ESB was used as the ion conducting phase in the composite cathode for both samples yet this change in activation energy is only observed in the sample where ESB was also present at the cathode/electrolyte interface.

Fig. 7 is a schematic diagram of the ORR at the LSM–ESB cathode. The overall ORR at the cathode and incorporation into the electrolyte is described in Kröger–Vink notation as:



Although various ORR mechanisms have been suggested, it is generally accepted that the oxygen reduction at the cathode can be

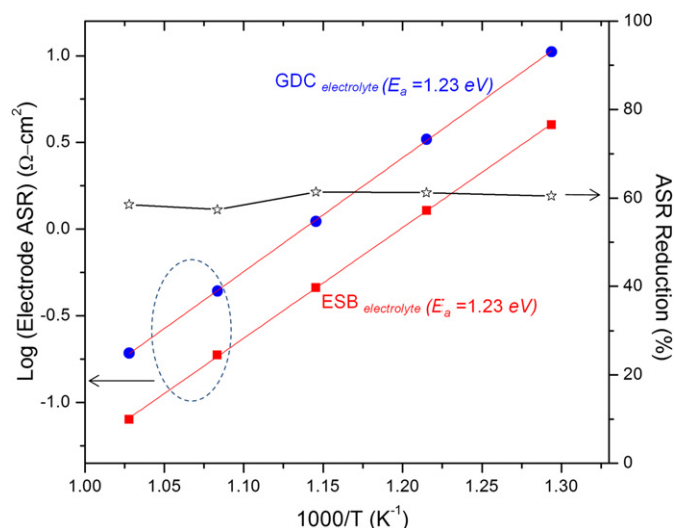


**Fig. 4.** ASR reduction percentage (blank stars) and electrode ASRs of LSM–ESB cathode on GDC (circles) and ESB (squares) electrolytes. The solid (red) lines show linear fits of the measured impedance data (For interpretation of the references to color in this figure legend, the reader is referred to the web version of this article.).

described with the most plausible rate-limiting steps as follows [44–46];

- Step 1:  $\text{O}_2 \rightarrow 2\text{O}_{\text{ad}}$  (dissociative adsorption)
- Step 2:  $\text{O}_{\text{ad}} + \text{e}' \rightarrow \text{O}'_{\text{ad}}$  (charge transfer)
- Step 3:  $\text{O}'_{\text{ad}} \rightarrow \text{O}'_{\text{TPB}}$  (surface diffusion)
- Step 4:  $\text{O}'_{\text{TPB}} + \text{e}' \rightarrow \text{O}''_{\text{TPB}}$  (charge transfer at TPB)
- Step 5:  $\text{O}''_{\text{TPB}} + \text{V}_{\text{O}}^{\cdot} \rightarrow \text{O}_{\text{O,electrolyte}}^{\times}$  (oxygen ion incorporation)

Fig. 7b and c aids in visualizing the simple ORR model suggested above at the LSM–ESB cathode on GDC and ESB electrolyte interfaces, respectively. For LSM–ESB on ESB (Fig. 7c) all of the TPBs are identical. Further, for LSM–ESB on ESB it is clear from Fig. 6 that the incorporation reaction at the LSM–ESB–gas TPBs is not rate limiting ( $R_H \ll R_L$ ). Moreover, the impedance results indicate that, from change in activation energy at 600 °C,  $R_H$  involves transport through ESB and thus does not distinguish between ESB in cathode composite structure and ESB interfacial layer (identical TPBs).

In contrast, for LSM–ESB on GDC (Fig. 7b) there are two different TPBs near the cathode/electrolyte interface and  $R_H \sim R_L$  (Fig. 6). In addition, there is another impedance at the ESB/GDC interface. These two impedances LSM–GDC–gas and ESB/GDC are greater than the LSM–ESB–gas TPB impedance and thus overshadow the ESB ionic conductivity contribution to the LSM–ESB  $R_H$  impedance.

However these two different mechanisms are in apparent contrast to the identical overall ASR activation energies, 1.23 eV, in Fig. 4. This can also be explained by the magnitude of the EIS components. For LSM–ESB on ESB the magnitude of  $R_L$  dominates over the temperature range investigated, indicating oxygen adsorption, dissociation, and/or surface diffusion are rate limiting steps. Moreover, the activation energy for  $R_L$  is 1.26 eV, which is comparable to overall ASR activation energy of 1.23 eV.

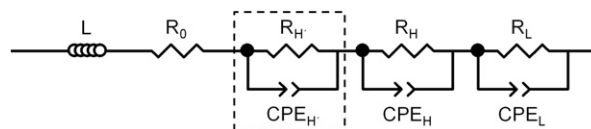


**Fig. 5.** Equivalent circuit used for fitting Nyquist plots.

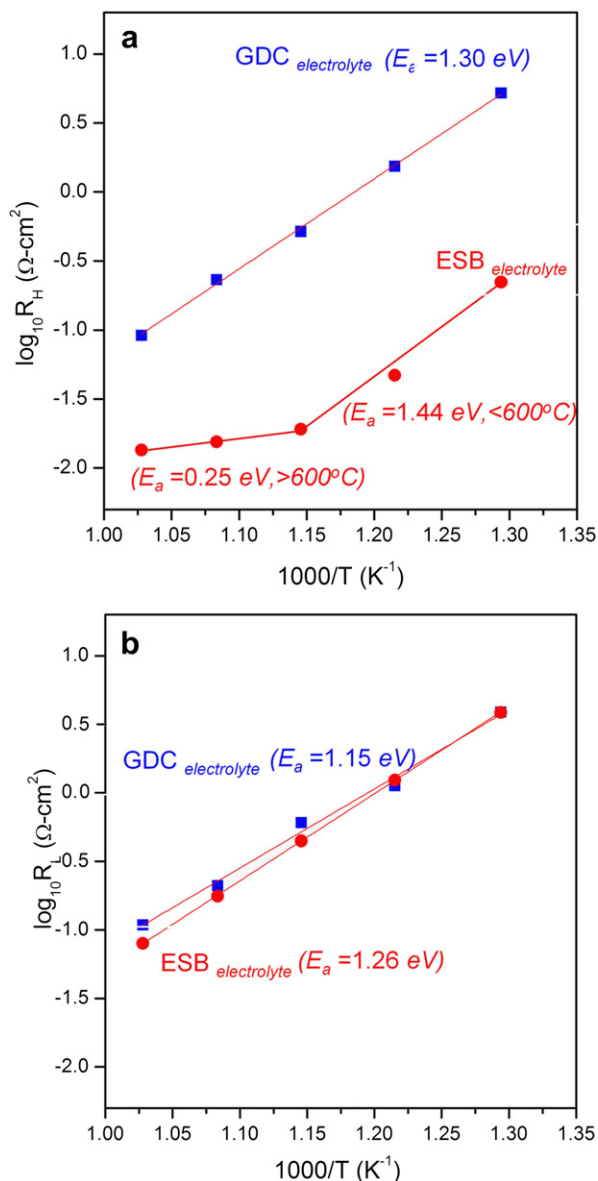


**Fig. 6.** Arrhenius plots for resistance of LSM-ESB cathode on GDC and ESB electrolytes at (a) high frequency ( $R_H$ ) and (b) low frequency ( $R_L$ ).

In contrast, for LSM-ESB on GDC the magnitude of  $R_H$  and  $R_L$  is essentially the same over the temperature range investigated, with  $R_H$  having an activation energy of 1.30 eV and  $R_L$  having an activation energy of 1.15 eV. Since the magnitudes are essentially the same neither component is rate limiting over this temperature range and the apparent activation energy is the combination of these two components. In fact, averaging these two activation energies results in 1.23 eV which is the observed apparent overall ASR activation energy.

### 3.4. SOFC performance

$I$ - $V$  measurements were conducted on anode-supported button cells in order to investigate the effect of LSM-ESB cathodes coupled to an interfacial ESB electrolyte layer on actual SOFC performance at lower temperatures. An ESB|GDC bilayered electrolyte cell was utilized due to the thermodynamic instability of the ESB electrolyte at low  $P_{\text{O}_2}$  conditions [27]. The cross-sectional SEM image of the

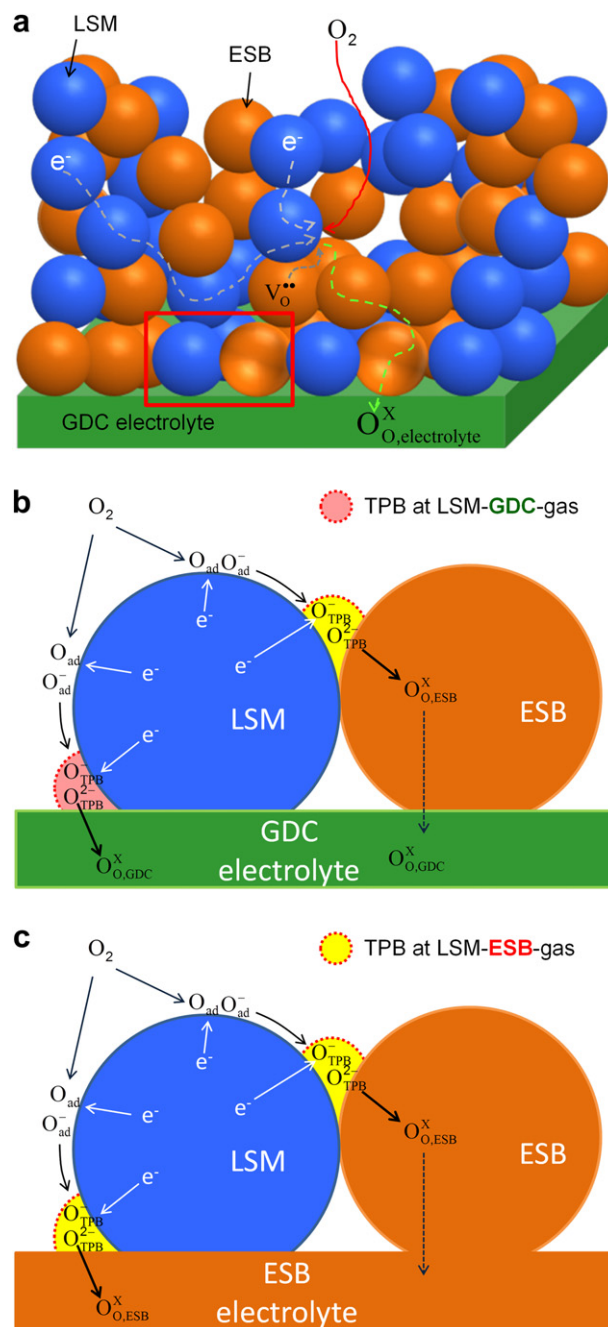


**Fig. 7.** Schematic diagrams of (a) overall ORR at LSM-ESB cathode with GDC electrolyte, (b) an ORR model at the cathode (LSM-ESB)/electrolyte (GDC) interface, and (c) at the cathode (LSM-ESB)/electrolyte (ESB) interface.

SOFC after testing is shown in Fig. 8a. The thin ( $\sim 2 \mu\text{m}$ ) and dense ESB electrolyte is shown between the GDC electrolyte and LSM-ESB cathode.  $I$ - $V$  curves of the cell with LSM-ESB on ESB|GDC at the temperature ranges from 450 to 650 °C are shown in Fig. 8b. The maximum power densities (MPDs) were 88, 185, 343, 667, and 1013  $\text{mW cm}^{-2}$  at 450, 500, 550, 600, and 650 °C, respectively.

### 3.5. LSM-ESB cathode performance comparison

A comparison of the cathodic ASR of LSM-ESB cathodes and several LSM-based cathodes with various electrolytes from the literature is shown in Fig. 9. Compared to the LSM-GDC cathode on

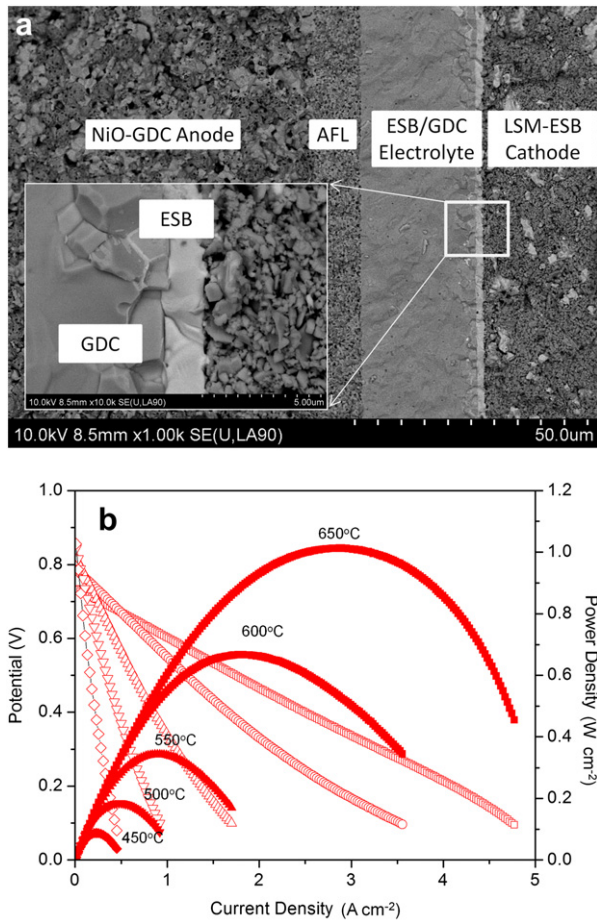


**Fig. 8.** (a) SEM images of cross-sectional view and (b) *I*–*V* characteristics at various temperatures for a SOFC with LSM–ESB cathode on ESB|GDC bilayered electrolyte.

YSZ electrolyte studied by Murray et al. [12], LSM–bismuth oxide cathodes on ceria or zirconia based electrolytes show  $\sim 7\times$  lower ASR at 600 °C ( $\sim 1 \Omega \text{ cm}^2$  vs  $\sim 7 \Omega \text{ cm}^2$ ), indicating that the addition of the faster ionic conducting phase into the cathode significantly reduces cathode polarization. Furthermore, use of ESB electrolyte

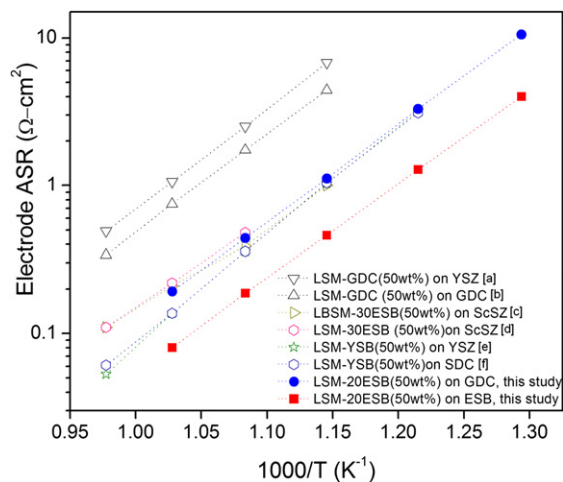


**Fig. 9.** Comparison of ASR for LSM-based composite cathodes with various electrolytes. [a],[b] – [12], [c] – [29], [d] – [33], [e] – [34], [f] – [31].

with LSM–ESB dramatically reduced the cathodic ASR ( $\sim 0.4 \Omega \text{ cm}^2$ ) by  $\sim 17.5\times$  compared to LSM–GDC on YSZ. This result clearly shows the effect of an interfacial ESB electrolyte on enhancing cathode performance due to improving the oxygen incorporation rate. It is also noted that our LSM–ESB cathode fabricated using solid-state synthesis and hand-mixing on the GDC electrolyte shows a comparable resistance (e.g.,  $\sim 1 \Omega \text{ cm}^2$  at 600 °C) compared to other LSM–bismuth oxide cathodes on ceria or zirconia based electrolytes (e.g.,  $\sim 0.9 \Omega \text{ cm}^2$  at 600 °C) although others used tailored microstructures with nanoscale bismuth oxides and/or LSM using wet chemical methods [29] or an infiltration process [31,34].

A comparison of MPDs for SOFCs with various LSM cathodes at low temperatures (450–650 °C) is shown in Fig. 10. The SOFC with our LSM–ESB cathode coupled to the interfacial ESB electrolyte layer shows the highest MPD for all temperatures. This result further demonstrates that the effect of the ESB electrolyte on LSM–ESB cathode polarization losses directly influences the SOFCs performance at LT, yielding a high maximum power density of over  $1 \text{ W cm}^{-2}$  at 650 °C. Moreover, the enhancing effect of the ESB electrolyte on LSM–ESB performance is even greater at low temperatures. Cathodic polarization losses are larger at lower temperature due to its thermally activated nature [5]. Therefore, the beneficial effect of the ESB electrolyte layer on cathode performance is emphasized when using LSM–ESB cathodes for low temperature SOFC application. To our knowledge, the obtained MPDs at the temperatures from 450 to 650 °C are the highest for any SOFCs using any LSM-based cathodes reported to date. Furthermore, this LSM–ESB cathode on an ESB electrolyte can be expected to produce much higher power density through optimization of the cathode microstructure as well as the bilayer electrolyte thickness and overall thickness ratio [47].

### 3.6. Stability

Long-term electrode ASR stability of the LSM–ESB cathode on ESB was measured using EIS at open circuit conditions (Fig. 11). The cathodic polarization of an LSM–ESB|ESB|LSM–ESB symmetric cell at 700 °C did not show any measurable degradation after 100 h, while the previously reported Ag–ESB cathode on the same ESB electrolyte showed significant decay at 650 °C [48]. This result indicates relatively high stability of the LSM–ESB cathode.

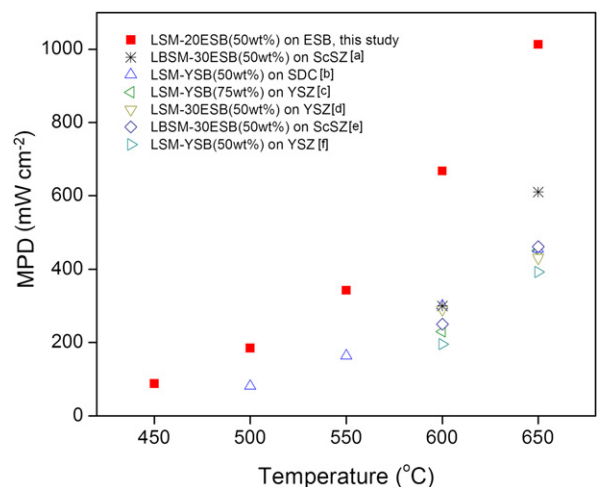


**Fig. 10.** Comparison of maximum power density of SOFCs using LSM–bismuth oxide based composite cathodes at temperatures from 450 to 650 °C. [a] – [32], [b] – [31], [c] – [37], [d] – [33], [e] – [36], [f] – [31].

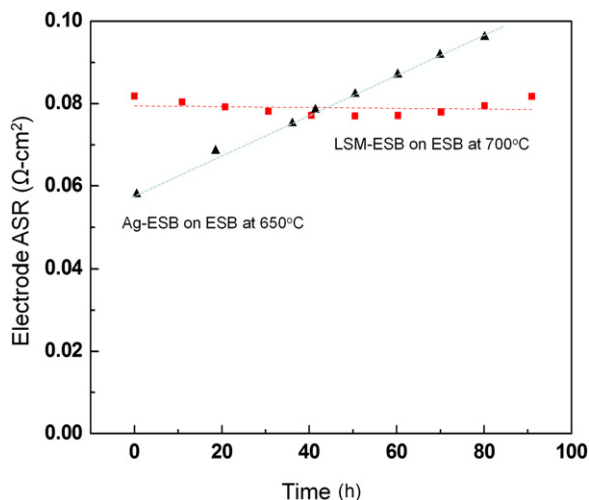


**Fig. 11.** Long-term stability results for LSM-ESB cathode on ESB electrolyte at 700 °C for 100 h in this study (squares) and Ag-ESB cathode on ESB electrolyte at 650 °C reported by Camaratta et al. (triangles) [48].

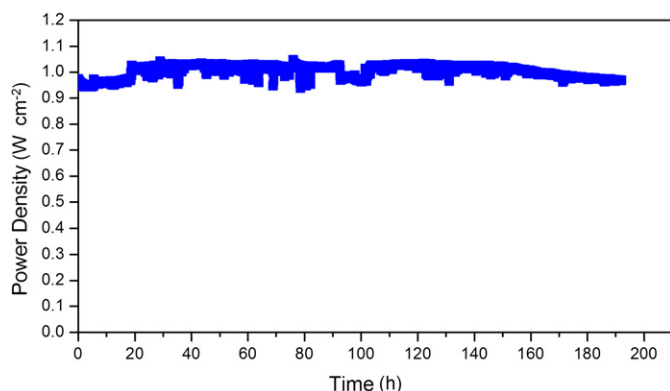


**Fig. 12.** Potentiostatic results at 650 °C for long-term stability of a SOFC with the LSM-ESB cathode on the ESB/GDC bilayered electrolyte.

The stability of SOFC performance with an LSM-ESB cathode coupled to an ESB/GDC bilayer electrolyte at 650 °C with 90 sccm of hydrogen (3% H<sub>2</sub>O) and dry air at anode and cathode, respectively, was determined potentiostatically under an applied voltage of 0.32 V (corresponding to MPD) as shown in Fig. 12. The high power density of  $\sim 1 \text{ W cm}^{-2}$  was retained for 200 h, further indicating high stability.

#### 4. Conclusions

Conventional high temperature LSM cathodes were prepared for low temperature SOFC application by pairing LSM with ESB in a composite cathode. Due to the enhanced oxygen ion incorporation rate at the cathode/electrolyte interface, the interfacial ASR of LSM-ESB cathodes on an ESB electrolyte was significantly reduced compared to that of the same cathode on a GDC electrolyte. Using an anode supported SOFC with the LSM-ESB cathode on an ESB/GDC bilayered electrolyte, the MPD produced at 650 °C was  $\sim 1013 \text{ mW cm}^{-2}$ , which is the highest reported MPD at this moderate temperature to date for any SOFCs using LSM-based cathodes. This study demonstrated that the performance of LSM-ESB cathodes is dramatically improved by the use of ESB electrolytes and is promising for development of SOFCs which operate at low temperatures.

#### Acknowledgments

This work was supported by Office of Naval Research (contract N00014-09-C-0467). Dr. K.T.L. acknowledges the Kwanjeong Educational Foundation scholarship.

#### References

- [1] N.Q. Minh, J. Am. Ceram. Soc. 76 (1993) 563–588.
- [2] E.P. Murray, T. Tsai, S.A. Barnett, Solid State Ionics 110 (1998) 235–243.
- [3] S.P. Yoon, J. Han, S.W. Nam, T.H. Lim, I.H. Oh, S.A. Hong, Y.S. Yoo, H.C. Lim, J. Power Sources 106 (2002) 160–166.
- [4] S.P. Jiang, J. Power Sources 124 (2003) 390–402.
- [5] B.C.H. Steele, Solid State Ionics 129 (2000) 95–110.
- [6] N.P. Brandon, S. Skinner, B.C.H. Steele, Annu. Rev. Mater. Res. 33 (2003) 183–213.
- [7] C.C. Kan, H.H. Kan, F.M. Van Assche, E.N. Armstrong, E.D. Wachsman, J. Electrochem. Soc. 155 (2008) B985–B993.
- [8] C.C. Kan, E.D. Wachsman, J. Electrochem. Soc. 156 (2009) B695–B702.
- [9] E.N. Armstrong, K.L. Duncan, E.D. Wachsman, J. Electrochem. Soc. 158 (2011) B283–B289.
- [10] E.N. Armstrong, K.L. Duncan, D.J. Oh, J.F. Weaver, E.D. Wachsman, J. Electrochem. Soc. 158 (2011) B492–B499.
- [11] T. Kenjo, S. Osawa, K. Fujikawa, J. Electrochem. Soc. 138 (1991) 349–355.
- [12] E.P. Murray, S.A. Barnett, Solid State Ionics 143 (2001) 265–273.
- [13] C.W. Tanner, K.Z. Fung, A.V. Virkar, J. Electrochem. Soc. 144 (1997) 21–30.
- [14] M. Juhl, S. Primdahl, C. Manon, M. Mogensen, J. Power Sources 61 (1996) 173–181.
- [15] Y.J. Leng, S.H. Chan, K.A. Khor, S.P. Jiang, J. Solid State Electrochem. 10 (2006) 339–347.
- [16] J.L. Li, S.R. Wang, Z.R. Wang, R.Z. Liu, X.F. Ye, X.F. Sun, T.L. Wen, Z.Y. Wen, J. Power Sources 188 (2009) 453–457.
- [17] N.X. Jiang, E.D. Wachsman, S.H. Jung, Solid State Ionics 150 (2002) 347–353.
- [18] N.M. Sammes, G.A. Tompsett, H. Nafe, F. Aldinger, J. Eur. Ceram. Soc. 19 (1999) 1801–1826.
- [19] M.J. Verkerk, M.W.J. Hammink, A.J. Burggraaf, J. Electrochem. Soc. 130 (1983) 70–78.
- [20] B.A. Boukamp, I.C. Vinke, K.J. Devries, A.J. Burggraaf, Solid State Ionics 32–33 (1989) 918–923.
- [21] B.A. Boukamp, Solid State Ionics 136 (2000) 75–82.
- [22] B.C.H. Steele, J.A. Kilner, P.F. Dennis, A.E. McHale, M. Vanhemert, A.J. Burggraaf, Solid State Ionics 18–9 (1986) 1038–1044.
- [23] A. Jaiswal, C.T. Hu, E.D. Wachsman, J. Electrochem. Soc. 154 (2007) B1088–B1094.
- [24] M. Camaratta, E. Wachsman, J. Electrochem. Soc. 155 (2008) B135–B142.
- [25] T. Takahashi, T. Esaka, H. Iwahara, J. Appl. Electrochem. 7 (1977) 299–302.
- [26] E.D. Wachsman, P. Jayaweera, N. Jiang, D.M. Lowe, B.G. Pound, J. Electrochem. Soc. 144 (1997) 233–236.
- [27] J.S. Ahn, D. Pergolesi, M.A. Camaratta, H. Yoon, B.W. Lee, K.T. Lee, D.W. Jung, E. Traversa, E.D. Wachsman, Electrochem. Commun. 11 (2009) 1504–1507.
- [28] J.S. Ahn, M.A. Camaratta, D. Pergolesi, K.T. Lee, H. Yoon, B.W. Lee, D.W. Jung, E. Traversa, E.D. Wachsman, J. Electrochem. Soc. 157 (2010) B376–B382.
- [29] J.L. Li, S.R. Wang, Z.R. Wang, R.Z. Liu, T.L. Wen, Z.Y. Wen, J. Power Sources 179 (2008) 474–480.
- [30] J.L. Li, S.R. Wang, X.F. Sun, R.Z. Liu, X.F. Ye, Z.Y. Wen, J. Power Sources 185 (2008) 649–655.
- [31] Z.Y. Jiang, L. Zhang, K. Feng, C.R. Xia, J. Power Sources 185 (2008) 40–48.
- [32] J. Li, S. Wang, R. Liu, T. Wen, Z. Wen, Fuel Cells 9 (2009) 657–662.
- [33] J.L. Li, S.R. Wang, Z.R. Wang, R.Z. Liu, T.L. Wen, Z.Y. Wen, J. Power Sources 194 (2009) 625–630.
- [34] Z.Y. Jiang, L. Zhang, L.L. Cai, C.R. Xia, Electrochim. Acta 54 (2009) 3059–3065.
- [35] Z.Y. Jiang, C.R. Xia, F. Zhao, F.L. Chen, Electrochem. Solid-State Lett. 12 (2009) B91–B93.
- [36] J.L. Li, S.R. Wang, Z.R. Wang, J.Q. Qian, R.Z. Liu, T.L. Wen, Z.Y. Wen, J. Solid State Electrochem. 14 (2010) 579–583.
- [37] Z. Jiang, Z. Lei, B. Ding, C. Xia, F. Zhao, F. Chen, Int. J. Hydrogen Energy 35 (2010) 8322–8330.
- [38] Q.S. Zhang, A. Hirano, N. Imanishi, Y. Takeda, K. Yamahara, J. Fuel Cell Sci. Technol. 6 (2009).
- [39] S. deSouza, S.J. Visco, L.C. DeJonghe, Solid State Ionics 98 (1997) 57–61.
- [40] K.T. Lee, D.W. Jung, M.A. Camaratta, J.S. Ahn, E.D. Wachsman, J. Power Sources 205 (2012) 122–128.
- [41] V.V. Kharton, E.N. Naumovich, V.V. Samokhval, Solid State Ionics 99 (1997) 269–280.
- [42] J.Y. Park, H. Yoon, E.D. Wachsman, J. Am. Ceram. Soc. 88 (2005) 2402–2408.
- [43] J.R. Smith, A. Chen, D. Gostovic, D. Hickey, D. Kundinger, K.L. Duncan, R.T. DeHoff, K.S. Jones, E.D. Wachsman, Solid State Ionics 180 (2009) 90–98.
- [44] F.H. vanHeuveln, H.J.M. Bouwmeester, J. Electrochem. Soc. 144 (1997) 134–140.
- [45] J.D. Kim, G.D. Kim, J.W. Moon, Y.I. Park, W.H. Lee, K. Kobayashi, M. Nagai, C.E. Kim, Solid State Ionics 143 (2001) 379–389.
- [46] X.J. Chen, K.A. Khor, S.H. Chan, J. Power Sources 123 (2003) 17–25.
- [47] E.D. Wachsman, K.T. Lee, Science 334 (2011) 935–939.
- [48] M. Camaratta, E. Wachsman, Solid State Ionics 178 (2007) 1242–1247.